# Structural phase transition and Goldstone-like mode in hexagonal $BaMnO_3$

Xuefeng Zhang,[1] Qi-Jun Ye,[1] and Xin-Zheng Li[1,2,*]

[1]*State Key Laboratory for Artificial Microstructure and Mesoscopic Physics, Frontier Science Center for Nano-optoelectronics and School of Physics, Peking University, Beijing 100871, People's Republic of China*

[2]*Collaborative Innovation Center of Quantum Matter, Peking University, Beijing 100871, People's Republic of China*

(Received 3 October 2020; revised 5 December 2020; accepted 22 December 2020; published 5 January 2021)

Using first-principles-based Hamiltonian, we show novel structural behaviors of hexagonal manganite $BaMnO_3$ at moderate low temperatures ($T$s). The structural change of $BaMnO_3$ occurring at ∼130 K is assigned to an improper transition between the low-$T$ ferroelectric phase with $P6_3cm$ symmetry and a high-$T$ nonpolar phase with $P6_3/mmc$ symmetry, induced by coupled softening of the $K_3$ and $\Gamma_2^-$ modes. Herein, the order parameters show unconventional behaviors, with the mode amplitude being order-disorder like and the mode phase being displacive. Optical Goldstone-like mode, implied by the Mexican-hat-like Born-Oppenheimer potential energy surface, is manifested in our simulations via tuning quantum fluctuations and lattice strains. As this mode can be enhanced by lowering the contribution of intersite interactions, we suggest an experimental detecting scheme by inducing a light active Γ-point mode strongly coupled to it.

DOI: 10.1103/PhysRevB.103.024101

## I. INTRODUCTION

Quantum effects of electrons usually play a central role on inducing nontrivial states of matters, e.g., superconductors, quantum criticality, and magnetism [1–3]. The much larger masses of nuclei than electrons mean that in standard theory they can be treated as classical particles. When the nuclear quantum effects (NQEs) are important, one often resorts to concepts like phonon to address the quantum nature of the nuclei within the harmonic or quasiharmonic approximations. Recently, advances in the technique of path integrals mean that thorough quantum descriptions of condensed matters with full anharmonicity are possible [4–7]. Along this route, NQEs were systematically studied in light element systems, e.g., high-pressure hydrogen [8–10], liquid water [11], water-solid surfaces [12,13], and hexagonal boron nitride [14]. Even in systems with heavy elements, there could be prominent NQEs, e.g., the quantum paraelectrics [6,15,16]. But compared with the quantum states induced by electrons, quantum states determined by NQEs are still rare.

The so-called hexagonal manganite $RMnO_3$ ($R$ = Dy-Lu, In, Y, or Sc), due to the nontrivial ferroelectric (FE) domain structures, are of broaden fundamental and technological interest [17–21]. One important property of them is that their FE polarization is not the primary order parameter which dominates the paraelectric (PE) to FE phase transition, but an improper parameter induced at low temperatures ($T$s) by coupling to the primary one. As a result, a Mexican-hat-like Born-Oppenheimer potential energy surface (BO-PES), which has six valleys as sixfold degenerate ground states exists and Goldstone-like mode was suggested [22]. The Goldstone mode, arising when a continuous symmetry is broken, is a concept originally used in particle physics [23,24]. It was characterized by frequency $\omega_{\mathbf{k}} \to 0$ in the $\mathbf{k} \to \mathbf{0}$ limit. In condense matters, it has been proposed in many isotropic systems, like Heisenberg ferromagnets [25], liquid crystals [26], and incommensurate structures [27]. In anisotropic crystal systems, it is hard for continuous symmetry to exist and the Goldstone mode is rarely reported [28–31]. Recently, such a mode has been predicted in two examples, $ErMnO_3$ and $InMnO_3$, based on analysis of their Mexican-hat-like BO-PES [22]. Rigorous determination of the nature of this mode, however, requires finite-$T$ simulations with anharmonicity and NQEs fully taken into account. But such theoretical studies are rare.

In this article, we investigate the finite-$T$ structural behaviors of such hexagonal manganite, using $BaMnO_3$ (BMO) as the targeting system. The structural changes happened during the phase transition of this material is rather unclear [32–35], and the barrier between the sixfold local minima of the BO-PES is low, so that it is very likely for the NQEs to be important at low-$T$s. We use the first-principles-based classical Monte Carlo (CMC) and path-integral Monte Carlo (PIMC) simulations as the basic technique. Our simulations first assign the phase transition occurring at ∼130 K to an improper FE transition between the low-$T$ FE phase with $P6_3cm$ symmetry and a high-$T$ nonpolar $P6_3/mmc$ phase. Then we focus on the local structural changes. The $T$-dependent distribution of the amplitude order parameter show order-disorder-like behavior during the transition, while the behavior of the phase parameter is displacive. This is a rather unconventional feature in the PE to FE phase transitions, only similar to the recently reported results for $YMnO_3$ in Ref. [36]. By introducing NQEs, our PIMC simulations imply that a long-wavelength optical Goldstone-like mode exists at low $T$s. However, the intersite coupling term in the Hamiltonian traps the system into one of the sixfold local minima of the BO-PES, preventing the

*xzli@pku.edu.cn

 

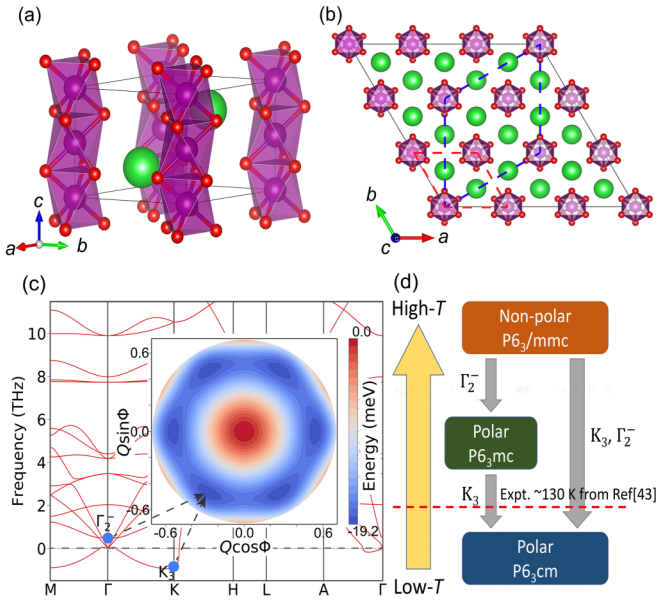


FIG. 1. (a) Crystal structure of nonpolar $P6_3/mmc$ $BaMnO_3$. The Ba, Mn, and O atoms are denoted by green, purple, and red balls, respectively. This custom holds for all figures of this manuscript. (b) The crystal lattice of polar $P6_3cm$ phase of $BaMnO_3$ (labeled by blue dashed lines) is 3 times than $P6_3/mmc$ phase (labeled by red dashed lines). (c) Phonon spectrum of $P6_3/mmc$ $BaMnO_3$. Blue circles denote $K_3$ and $\Gamma_2^-$ mode which dominate $BaMnO_3$'s structural phase transition. Inset panel shows the Mexican-hat-like BO-PES of $BaMnO_3$. The sixfold valleys on the BO-PES are induced by the coupling between $K_3$ and $\Gamma_2^-$ modes. (d) The relationship between $P6_3/mmc$, $P6_3mc$, and $P6_3cm$ phases. The red dashed line denotes the structural phase transition observed by experiments at around 130 K [34].

emergence of this Goldstone-like mode. To avoid this, one can resort to light activation by employing the coupling between this Goldstone-like mode and other light-active phonon modes in experiments. These results settle the dispute of BMO's phase transition in the viewpoint of the first-principles-based CMC/PIMC simulations. They also suggest that BMO is a new example in which the quantum nature of nuclei induce novel phenomena, even in the FE phase, which is seldom reported.

This article is organized as follows. In Sec. II, we present the methodology of constructing the effective lattice Hamiltonian. The computational details for obtaining the model coefficients and for performing the CMC/PIMC simulations are also provided. In Sec. III, we discuss the results on the $T$ dependence of order parameters and the local structural changes of $BaMnO_3$ and show that the quantum fluctuations of nuclei can induce the emergence of the Goldstone-like mode. The conclusions are summarized in Sec. IV.

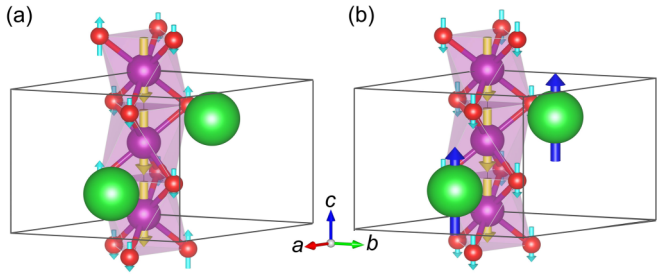


FIG. 2. Visualization of phonon eigenvectors of $P6_3/mmc$-$BaMnO_3$ for (a) the nonpolar $K_3$ mode and (b) the improper FE $\Gamma_2^-$ mode.

## II. METHODS

### A. Model Hamiltonian

Unlike $ErMnO_3$ and $InMnO_3$, whose structures contain corner-sharing Mn-O trigonal bipyramids, BMO's structure is characterized by face-sharing Mn-O octahedra separated by Ba ions [Fig. 1(a)]. At ~130 K and ambient pressure, BMO was believed to undergo a structural phase transition induced by the softening of the noncentrosymmetric, nonpolar, Brillouin zone-boundary $K_3$ mode [Fig. 1(b)]. This structural instability of high-$T$ nonpolar $P6_3/mmc$ phase can be perceived from its phonon spectrum [Fig. 1(c)]. The $K_3$ mode is composed by Mn and O atoms' vibrations along the $c$ axis [Fig. 2(a)], which can be described using an amplitude parameter $Q$ and a phase parameter $\Phi$. Besides $K_3$, the $\Gamma_2^-$ mode at the Brillouin zone center should also be noted. This FE $\Gamma_2^-$ mode, denoted by $P$, is consisted by relative vibration between the Mn-O octahedra and the Ba ions along the $c$ axis [Fig. 2(b)]. The $K_3$ mode shows no evident dependence on the phase parameter $\Phi$, but the coupling between the $K_3$ and $\Gamma_2^-$ modes raises sixfold degenerate valleys of the BO-PES at $\Phi = 2n\pi/6$ with $n = 0, 1, \ldots, 5$ [the inset of Fig. 1(c)]. As a result, the low-$T$ structure of BMO possesses the $P6_3cm$ symmetry.

To understand the structural changes of BMO during the phase transition, we resort to first-principles-based CMC and PIMC simulations. Compared with previous theoretical studies of this material based on the Landau theory, which are static [33], our simulations allow the finite-$T$ thermal effects and NQEs to be addressed [4,5,8,11,12], with full anharmonicity taken into account. To approach the thermodynamic limit, large supercells beyond the reach of pure first-principles simulations were used [6,16]. This is achieved by resorting to an accurate and computationally affordable effective model. The low-energy characteristics of BMO, dominated by the $K_3$ and $\Gamma_2^-$ modes as discussed above, mean that a Landau-type effective Hamiltonian,

$$\begin{aligned} H &= H_{\text{local}} + H_{\text{inter}} \\ &= \sum_i \left[a_1 Q_i^2 + b_1 Q_i^4 + g P_i Q_i^3 \cos(3\Phi_i) + g' P_i^2 Q_i^2 + a_2 P_i^2\right] \\ &\quad + \sum_{\lambda=x,z} \left( \frac{J_Q^\lambda}{4} \sum_{i\neq j} \left\{ (Q_i - Q_j)^2 + 2Q_i^2 [1 - \cos(\Phi_i - \Phi_j)] \right\} \right. \\ &\quad \left. + \frac{J_P^\lambda}{4} \sum_{i\neq j} (P_i - P_j)^2 \right), \end{aligned} \tag{1}$$

can be defined. The other phonon modes, which are not related to the structural phase transition directly, are neglected. The procedure outlined in a previous work by Skjærvø *et al.* on

$YMnO_3$ is adopted for the construction of this Hamiltonian [36], using a free-energy expansion similar to the suggestions of Varignon *et al.* [33]. The indices $i$, $j$ denote lattice sites, $Q$ and $\Phi$ represent the amplitude and the phase of the $K_3$ mode, and $P$ means the amplitude of the $\Gamma_2^-$ mode. The $H_{\text{local}}$ term is the on-site energy. The soft $K_3$ mode is described by a quartic function. The $\Gamma_2^-$ mode is positive and real when calculating phonon spectrum using experimental lattice constants, but imaginary when using first-principles optimized ones. Therefore, we tried simulations with the $\Gamma_2^-$ mode being treated as a quadratic function in the former case, and as a quartic function (add a $b_2 P_i^4$ term) in the latter case. The $K_3$-$\Gamma_2^-$ coupling terms reflect the improper FE nature, which is characteristic of hexagonal manganites [36,37]. To obtain the coefficients of the on-site part of our model Hamiltonian, we fit it to the first-principles BO-PES along the $K_3$ and $\Gamma_2^-$ phonon eigenvectors. The $H_{\text{inter}}$ term is the intersite part of our model, which reflects the energy change when the configuration of the order parameters (i.e., $P$, $Q$, and $\Phi$) deviates from the structural ground state. To obtain the stiffness parameters, $J_P^\lambda$ and $J_Q^\lambda$, we follow Refs. [36,37]. All these parameters are provided in the Supplemental Material [38].

### B. First-principles calculations

The DFT calculations were performed using the Vienna Ab initio Simulation Package [39,40], with PBEsol+U functional chosen for the description of the electronic exchange-correlation interactions [41,42]. The plane-wave cut-off energy is 500 eV. Concerning the Brillouin zone integration, we set the spacing between $\mathbf{k}$ points to 0.12 $\text{Å}^{-1}$. The on-site Coulomb interaction parameters are specified with $U = 4.52$ eV, which is determined by linear response [43]. All first-principles calculations are spin-polarized with the so-called A-type antiferromagnetic configuration in which spins on the same layer parallel with the *ab* plane are parallel to each other, and those along the *c* axis have opposite directions. Structural relaxation is performed with a conjugated-gradient algorithm, until the Hellmann-Feynman forces on each atom are less than 0.1 meV $\text{Å}^{-1}$. The phonon eigenenergies and eigenvectors are given by PHONOPY [44], using a $3 \times 3 \times 2$ supercell.

### C. Monte Carlo simulations

When the model Hamiltonian is constructed, we perform CMC and PIMC to simulate the finite-$T$ properties. Comparisons between results obtained from these two series of simulations allow the NQEs to be addressed in a very clean manner [6].

In the path-integral representation of quantum mechanics, a $N$-particles quantum mechanical partition function $Z = \text{Tr}[e^{-\beta \hat{H}}]$ is mapped to a $N \times N_s$-particles classical partition function [45] of a polymer through

$$Z_{\text{PI}} = \lim_{N_s \to \infty} \left[ \prod_{i=1}^{N} \left( \frac{m_i N_s}{2\beta\pi\hbar^2} \right)^{\frac{dN_s}{2}} \right] \int \cdots \int \left( \prod_{j=1}^{N_s} \prod_{i=1}^{N} d\mathbf{x}_j^i \right) \times e^{-\beta \sum_{j=1}^{N_s} \left[ \sum_{i=1}^{N} \frac{1}{2} m_i \omega_0^2 (\mathbf{x}_j^i - \mathbf{x}_{j-1}^i)^2 + \frac{1}{N_s} V(\mathbf{x}_j^1, \ldots, \mathbf{x}_j^N) \right]}. \tag{2}$$

Here $N_s$ is the number of slices for the sampling of the imaginary time $\beta = 1/(k_B T)$, $N$ is the number of particles in the realistic polyatomic system, $m_i$ is the mass of the $i$th particle, $d$ is the dimension of coordinate $\mathbf{x}$, and $\omega_0$ equals $\sqrt{N_s}/(\beta\hbar)$. The "classical polymer" is constructed using $N_s$ images of the realistic polyatomic system. The mapping ensures that conventional Monte Carlo or molecular dynamics simulations can be performed for this artificial "classical polymer," so that NQEs can be addressed rigorously for finite-$T$ statistical properties [4–6,8,10,16]. Within each image, the interatomic interaction in realistic system is adopted through $V(\mathbf{x}_j^1, \ldots, \mathbf{x}_j^N)$ in Eq. (2). In between the neighboring ($j$-1)th and $j$th images, the same atoms are connected by a spring which causes a potential energy of $\frac{1}{2} m_i \omega_0^2 (\mathbf{x}_j^i - \mathbf{x}_{j-1}^i)^2$ in Eq. (2). In the language of path integral, it actually corresponds to the kinetic energy along the path of the imaginary time.

The sampling of the "classical polymer" in Eq. (2) altogether give rise to NQEs such as zero-point motion and quantum tunneling. In our case, we treat the $K_3$ and $\Gamma_2^-$ modes on each site as two particles. The realistic interatomic interaction $V(\mathbf{x}_j^1, \ldots, \mathbf{x}_j^N)$ in Eq. (2) is described using Eq. (1), which corresponds to specific spatial configurations of the BMO supercell. The order parameters $(x_i^{K_3}, y_i^{K_3}) = (Q_i \cos\Phi_i, Q_i \sin\Phi_i)$ and $x_i^{\Gamma_2^-} = P$ are treated as the coordinates $\mathbf{x}_i$ of the two particles. Their effective masses are defined as $M_{\text{eff}} = \sum_i m_i \xi_i^2$, where $\xi$ denotes the vector describing the collective motion along $K_3$ or $\Gamma_2^-$ mode, and $m_i$ means the atomic mass of the corresponding vector components.

To ensure that the thermodynamic limit is reached, our simulations were performed on a $16 \times 16 \times 16$ supercell, which contains more than hundreds of thousands of atoms in real material. This is sheer impractical for pure *ab initio* calculations. We performed $\mathcal{O}(10^6)$ Monte Carlo sweeps (MCS) for thermalization and $\mathcal{O}(10^7)$ MCS for statistics. To study the $T$ dependence and the competition between the $K_3$ and $\Gamma_2^-$ mode, we treat all the order parameters $P$, $Q$, and $\Phi$ as independent variables in our CMC simulations. Moreover, to perform PIMC simulations, we use $TN_s = 1,024$ to keep a small Trotter error. The bisection algorithm was adopted to improve the sampling efficiency [46].

## III. RESULTS

### A. Structural phase transition

Recent theoretical and experimental studies believe that the low-$T$ structure of BMO is a FE $P6_3cm$ phase. But there is no consensus about its high-$T$ structure above ~130 K [32–35]. Two main candidates exist, i.e., a nonpolar $P6_3/mmc$ phase and a polar $P6_3mc$ phase [Fig. 1(d)]. The $P6_3/mmc$ phase lies at the center of the Mexican hat, with the magnitudes of both the $K_3$ and the $\Gamma_2^-$ modes being zero. In the first scenario, the $K_3$ mode freezes at decreasing $T$s from the high-$T$ $P6_3/mmc$ phase. When a finite $K_3$ mode appears, the $\Gamma_2^-$ become unstable and acquire nonzero amplitude due to $K_3$-$\Gamma_2^-$ coupling. Then the low-$T$ $P6_3cm$ phase becomes FE. Besides this, it could also happen that the $K_3$ mode disappears at ascending $T$s from the low-$T$ $P6_3cm$ phase, followed by the disappearance of $\Gamma_2^-$. Then the structural phase transition

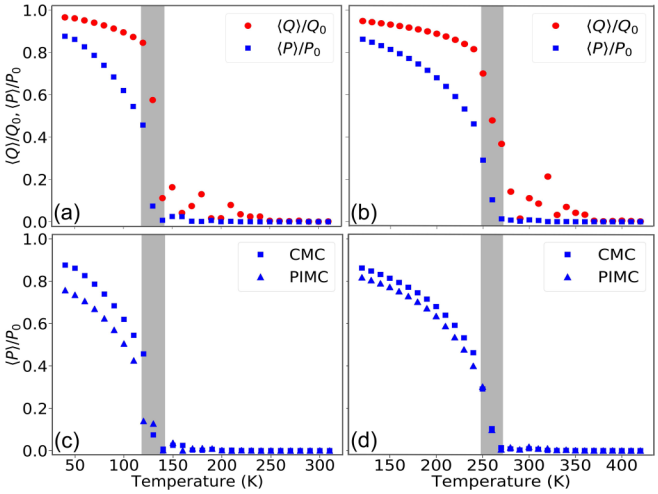


FIG. 3. Temperature dependence of order parameters that dominate the structural phase transition of $BaMnO_3$. Blue squares denote the the expectation value of $\Gamma_2^-$ mode and red circles denote the expectation value of $K_3$ mode. (a) CMC results performed on BMO with experimental lattice constants and (b) with first-principles optimized lattice constants. (c) PIMC results performed on BMO with experimental lattice constants and (d) PIMC results with first-principles optimized lattice constants.

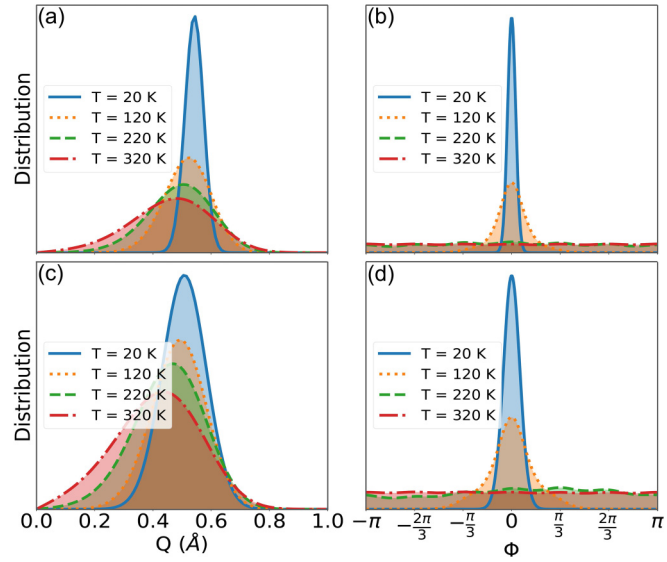


FIG. 4. Distributions of $Q$ (a) and $\Phi$ in (b) at different temperatures obtained by CMC simulations, and distributions of $Q$ (c) and $\Phi$ in (d) at different temperatures obtained by PIMC simulations.

at ∼130 K can happen between the low-$T$ $P6_3cm$ phase and the intermediate-$T$ $P6_3mc$ phase [the left route in Fig. 1(d)]. Therefore, the puzzle of BMO's structural phase transition at ∼130 K can be transformed to whether the $\Gamma_2^-$ mode still exists when the $K_3$ mode disappears.

We first performed CMC simulations to study the $T$ dependence of the $K_3$ and $\Gamma_2^-$ modes. Since the eigenstate energy of the $\Gamma_2^-$ mode is sensitive to the lattice constants, both the experimental and first-principles optimized lattice constant-based simulations were carried out. In these simulations, all the order parameters, i.e., $P$, $Q$, and $\Phi$, are treated as independent variables. The results are shown in Figs. 3(a) and 3(b). Blue squares denote the expectation value $\langle P\rangle$ of the $\Gamma_2^-$ mode, and red circles denote the expectation value $\langle Q\rangle = \sqrt{\langle Q_i \cos\Phi_i\rangle^2 + \langle Q_i \sin\Phi_i\rangle^2}$ of the $K_3$ mode. We choose the units as $P_0$ and $Q_0$, which are the solutions of $\partial H/\partial P = 0$ and $\partial H/\partial Q = 0$ in Eq. (1). With experimental lattice constants, both $\langle P\rangle$ and $\langle Q\rangle$ have finite values when $T < 140$ K, then vanish when $T > 140$ K. This is an obviously evidence of a structural phase transition, and that the low-$T$ phase of BMO has $P6_3cm$ symmetry with ferroelectricity. The appearance of finite $\langle Q\rangle$ is at slightly higher $T$ than $\langle P\rangle$. In other words, $\langle P\rangle$ cannot exist independently when $\langle Q\rangle$ disappears. In simulations with first-principles-based lattice constants, this feature holds at a larger critical $T$, due to the fact that the overestimated lattice constants obtained by first-principles calculations make the barriers on BMO's BO-PES higher. Such an improper FE nature is also shown in our first-principles calculations, which we provided in the Supplemental Material [38]. The PIMC results are close to the CMC ones, as shown in Figs. 3(c) and 3(d), indicating that NQEs have a negligible influence on $T_C$.

To summarize, in the viewpoint of CMC/PIMC simulations combined with a first-principles-based effective Hamiltonian, the structural phase transition of BMO is a transition from a high-$T$ nonpolar $P6_3/mmc$ phase to a low-$T$ polar $P6_3cm$ phase. This transition, therefore, is an improper FE transition, which means that the raise of the nonpolar $K_3$ mode is the prime reason of structural phase transition and the ferroelectricity induced by $\Gamma_2^-$ mode is a secondary effect. This result is consistent with a previous first-principles-based Landau theory study [33] and an early neutron powder diffraction experiment [32] but different from the conclusion drawn in some recent experimental studies [34,35]. We note, however, that the $P6_3/mmc$ structure and $P6_3mc$ structure are so close to each other that it is very difficult for them to be distinguished clearly by experiments, due to the inevitable experimental error, such as leakage current in the pyrocurrent measurements [35]. Therefore, it is fair to say that theoretical results of the high-$T$ BMO structure are consistent. Debates exist in their comparison with some experimental studies. Our study gives a finite-$T$ phase diagram of BMO using first-principle-based CMC/PIMC simulations, with anharmonicity and NQEs fully taken into account, which provides a reference for further theoretical and experimental studies.

### B. Local structure

With the nature of the phase transition clarified, we go to the details of the structural changes happened during this phase transition. This is done by analyzing the distributions of the order parameters $Q$ and $\Phi$. The average structure of BMO at $T > T_C$ is $P6_3/mmc$, so that the macroscopic expectation value of the amplitude of the $K_3$ mode, i.e., $\langle Q\rangle$, vanishes at high $T$s. The distribution of $Q_i$ has a peak at finite value when $T < T_C$. This peak remains at $T > T_C$, which is broadened due to the influence of thermal fluctuations [shown in Fig. 4(a)]. The distribution of phase $\Phi_i$, on the other hand, shows a single peak at low $T$, meaning that the system locates on one of

the six valleys on the BO-PES. This distribution broadens on heating and finally becomes flat between all $\Phi_i$s when $T > T_C$ [shown in Fig. 4(b)]. Therefore, the amplitude order parameter $Q$ of the $K_3$ mode is order-disorder like, but the phase $\Phi$ is displacive. This is unconventional for structural phase transitions, similarly to the recently reported results of $YMnO_3$ in Ref. [36]. Although the average structure of BMO has a $P6_3/mmc$ symmetry at high $T$, the local structure can locate at anywhere on the brim of the Mexican-hat-like BO-PES. The distributions of $Q$ and $\Phi$ obtained by PIMC are shown in Figs. 4(c) and 4(d), respectively. There are no qualitative changes, except for the fact that the distributions are further broadened due to the inclusion of NQEs. This feature is relevant to the Goldstone-like mode, as we will discuss in detail in next section.

Such behavior is also possibly the reason why previous experiments cannot rule out high-$T$ polar phase directly [35]. Since the local structure can locate at anywhere on the brim of the Mexican-hat-like BO-PES and part of these positions are corresponding to polar phases, some signatures originating from local polar structures might be caught. Higher precision experiments are required to confirm the high-$T$ structure of BMO. Moreover, the method based on pair distribution function analysis of neutron total scattering experiment, which is shown by previous work about $YMnO_3$ [36], might be useful to confirm such an unconventional behavior of BMO's local structure.

### C. Goldstone-like mode

With growing thermal fluctuations, the system can get rid of the constraints and escape from the valleys of the local Mexican-hat-like BO-PES. As a result, the phase parameter $\Phi$ can be an arbitrary value between 0 and $2\pi$ when $T > T_C$, indicating the arising of a U(1) symmetry [see Fig. 5(a)]. The existence of the U(1) symmetry implies Goldstone-like mode, wherein varying $\Phi$ globally costs no external energy. To highlight the collective feature of the Goldstone mode, we retain the Hamiltonian to $\mathbf{k} \to \mathbf{0}$, i.e., ruling out intersite interactions $H_{\text{inter}}$. The remaining part $H_{\text{local}}$ presents a Mexican-hat BO-PES with very low barriers between its six discrete ground states on the brim. Naturally, a question concerning how NQEs can impact on the Goldstone mode arises. To answer this question, we perform CMC and PIMC simulations at 2 K to minimize the contribution from thermal fluctuations. The PIMC results are shown in Figs. 5(b)–5(d) with 0.35%, 0%, and −0.35% strain along $c$ axis, respectively, and the corresponding CMC results are given in their insets. On decreasing the strain, the CMC results show a unified picture of the sixfold degenerate discrete minima, while the PIMC ones show a tendency to continuous degenerate ground state. A ringlike histogram appears at −0.35%, meaning that in this case the Goldstone-like mode is induced purely by NQEs.

It should be noted that a flattening due to NQEs of such an energy landscape was rarely reported. NQEs are conventionally known to play important roles only in systems consisting of light elements [4,5,7–11,14] or in quantum paraelectric systems [6,15,16]. BMO is an new example of heavy element system, where the barriers between the local minima on the brim of BO-PES are low and the structures associated with these local minima are close. These features result in invalidity of the conventional harmonic or quasiharmonic treatments for the quantum behaviors of the nuclei. Thus, path-integral methods beyond the harmonic or quasiharmonic approximations are required [4–6,16]. Besides these, the FE nature of the phase at 2 K when NQEs flatten the BO-PES is also nontrivial, since in quantum paraelectric systems the NQEs change the picture of the system in the PE phase. Experimental identification of this feature using methods like isotope substitution is highly desired.

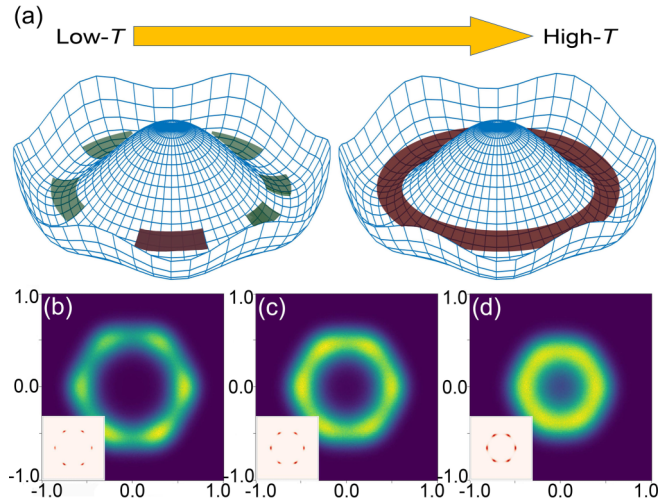


FIG. 5. (a) Schematic of local values of the order parameter at both sides of the structural phase transition. The system's symmetry is transform from a sixfold discreted symmetry to a U(1) symmetry on increasing $T$s. [(b)–(d)] Histogram obtained by PIMC to reflect the free-energy surface of $BaMnO_3$ with 0.35%, 0%, −0.35% strain along $c$ axis. Inset panels in (b)–(d) are the corresponding CMC results.

In Fig. 4, we have shown that the system will be trapped into one of the six valleys if the full Hamiltonian is used. Intersite couplings prevent the local parameters on each sites from changing independently, and the large number of particles in system makes the scenario when local parameters on all sites change synchronically unlikely. Therefore, it is fair to say that the contribution from $H_{\text{inter}}$ results in the fundamental difference between the Goldstone-like mode as described in Fig. 5 and the trapped structure as reflected by Fig. 4. Practically, however, we note that the Goldstone-like mode in Fig. 5 is obtained by ignoring $H_{\text{inter}}$. For a realistic system where all interactions exist, one might be able to achieve it by lowering the contribution from $H_{\text{inter}}$. For example, if a light active Γ-point mode strongly coupled to the Goldstone-like mode is induced, e.g., Higgs-like mode, one could detect the Goldstone-like mode experimentally. In fact, a recent study has suggested this mechanism for $InMnO_3$, which has the same symmetry as BMO in both sides of its structural phase transition [47]. In the end, we note that the barrier between valleys along the brim of the Mexican-hat BO-PES depends on the lattice constant. Therefore, one may expect that the NQEs induced Goldstone-like mode may be induced by solely tuning the strain. But as we have shown, the strong coupling

between neighboring unit cells in realistic system means that this is unlikely. Inducing this mode by its coupling with some optical excitations is a more practical scheme.

## IV. CONCLUSION

In conclusion, we performed CMC/PIMC simulations combined with a Landau-type effective Hamiltonian based on first-principles calculations. Our results show that the structural phase transition of BMO at ∼130 K is an improper transition from a nonpolar $P6_3/mmc$ phase to a polar $P6_3cm$ phase. The local structure change of BMO during this transition is unconventional due to the fact that the amplitude order parameter $Q$ of the $K_3$ mode is order-disorder like, but the phase $\Phi$ is displacive. At low $T$s, NQEs can induce a Goldstone-like mode with the help of strain, which could be detected by light-matter interactions. Like the quantum paraelectric phase, we believe that BMO is another example in which quantum fluctuations of nuclei induce novel states in condensed matters, even when it is ferroelectric. We hope this discovery can stimulate more experimental and theoretical studies on BMO, and on new states of matter originating from the quantum nature of nuclei in a wider range of condensed matter systems.

## ACKNOWLEDGMENTS

The authors are supported by the National Basic Research Programs of China under Grant No. 2016YFA0300901; the National Science Foundation of China under Grants No. 11774003, No. 11934003, and No. 11634001; Beijing Natural Science Foundation under Grant No. Z200004; and the Strategic Priority Research Program of the Chinese Academy of Sciences under Grant No. XDB33010400. The computational resources were provided by the supercomputer center in Peking University, China.

[1] M. R. Norman, Science. **332**, 196 (2011).
[2] S. Sachdev, Science. **288**, 475 (2000).
[3] Y. Zhou, K. Kanoda, and T.-K. Ng, Rev. Mod. Phys. **89**, 025003 (2017).
[4] D. Marx and M. Parrinello, J. Chem. Phys. **104**, 4077 (1996).
[5] M. E. Tuckerman, D. Marx, M. L. Klein, and M. Parrinello, J. Chem. Phys. **104**, 5579 (1996).
[6] W. Zhong and D. Vanderbilt, Phys. Rev. B **53**, 5047 (1996).
[7] H. Liu, Y. Yuan, D. Liu, X.-Z. Li, and J. Shi, Phys. Rev. Research **2**, 013340 (2020).
[8] J. Chen, X.-Z. Li, Q. Zhang, M. I. J. Probert, C. J. Pickard, R. J. Needs, A. Michaelides, and E. Wang, Nat. Commun. **4**, 2064 (2013).
[9] I. Errea, M. Calandra, C. J. Pickard, J. R. Nelson, R. J. Needs, Y. Li, H. Liu, Y. Zhang, Y. Ma, and F. Mauri, Nature **532**, 81 (2016).
[10] X.-W. Zhang, E.-G. Wang, and X.-Z. Li, Phys. Rev. B **98**, 134110 (2018).
[11] J. A. Morrone and R. Car, Phys. Rev. Lett. **101**, 017801 (2008).
[12] X.-Z. Li, M. I. J. Probert, A. Alavi, and A. Michaelides, Phys. Rev. Lett. **104**, 066102 (2010).
[13] J. Guo, J.-T. Lu, Y. Feng, J. Chen, J. Peng, Z. Lin, X. Meng, Z. Wang, X.-Z. Li, E.-G. Wang, and Y. Jiang, Science. **352**, 321 (2016).
[14] T. Q. P. Vuong, S. Liu, A. Van der Lee, R. Cuscó, L. Artús, T. Michel, P. Valvin, J. H. Edgar, G. Cassabois, and B. Gil, Nat. Mater. **17**, 152 (2018).
[15] K. A. Müller and H. Burkard, Phys. Rev. B **19**, 3593 (1979).
[16] X. Zhang, Q.-J. Ye, H. Xiang, and X.-Z. Li, Phys. Rev. B **101**, 104102 (2020).
[17] S.-Z. Lin, X. Wang, Y. Kamiya, G.-W. Chern, F. Fan, D. Fan, B. Casas, Y. Liu, V. Kiryukhin, W. H. Zurek, C. D. Batista, and S.-W. Cheong, Nat. Phys. **10**, 970 (2014).
[18] T. Choi, Y. Horibe, H. T. Yi, Y. J. Choi, W. Wu, and S.-W. Cheong, Nat. Mater. **9**, 253 (2010).
[19] J. A. Mundy, J. Schaab, Y. Kumagai, A. Cano, M. Stengel, I. P. Krug, D. M. Gottlob, H. Doğanay, M. E. Holtz, R. Held, Z. Yan, E. Bourret, C. M. Schneider, D. G. Schlom, D. A. Muller, R. Ramesh, N. A. Spaldin, and D. Meier, Nat. Mater. **16**, 622 (2017).
[20] N. Fujimura, T. Ishida, T. Yoshimura, and T. Ito, Appl. Phys. Lett. **69**, 1011 (1996).
[21] S. M. Griffin, M. Lilienblum, K. T. Delaney, Y. Kumagai, M. Fiebig, and N. A. Spaldin, Phys. Rev. X **2**, 041022 (2012).
[22] Q. N. Meier, A. Stucky, J. Teyssier, S. M. Griffin, D. van der Marel, and N. A. Spaldin, Phys. Rev. B **102**, 014102 (2020).
[23] J. Goldstone, Nuovo Cimento. **19**, 154 (1961).
[24] J. Goldstone, A. Salam, and S. Weinberg, Phys. Rev. **127**, 965 (1962).
[25] P. Böni, M. Hennion, and J. L. Martínez, Phys. Rev. B **52**, 10142 (1995).
[26] F. Gouda, K. Skarp, and S. T. Lagerwall, Ferroelectrics **113**, 165 (1991).
[27] A. D. Bruce and R. A. Cowley, J. Phys. C Solid State Phys. **11**, 3609 (1978).
[28] C. A. Kendziora, I. A. Sergienko, R. Jin, J. He, V. Keppens, B. C. Sales, and D. Mandrus, Phys. Rev. Lett. **95**, 125503 (2005).
[29] J. C. Petersen, M. D. Caswell, J. S. Dodge, I. A. Sergienko, J. He, R. Jin, and D. Mandrus, Nat. Phys. **2**, 605 (2006).
[30] S. M. Nakhmanson and I. Naumov, Phys. Rev. Lett. **104**, 097601 (2010).
[31] A. Marthinsen, S. M. Griffin, M. Moreau, T. Grande, T. Tybell, and S. M. Selbach, Phys. Rev. Materials **2**, 014404 (2018).
[32] E. J. Cussen and P. D. Battle, Chem. Mater. **12**, 831 (2000).
[33] J. Varignon and P. Ghosez, Phys. Rev. B **87**, 140403(R) (2013).
[34] T. N. Stanislavchuk, A. P. Litvinchuk, R. Hu, Y. H. Jeon, S. D. Ji, S.-W. Cheong, and A. A. Sirenko, Phys. Rev. B **92**, 134308 (2015).
[35] S. Kamba, D. Nuzhnyy, M. Savinov, P. Tolédano, V. Laguta, P. Brázda, L. Palatinus, F. Kadlec, F. Borodavka, C. Kadlec, P. Bednyakov, V. Bovtun, M. Kempa, D. Kriegner, J. Drahokoupil, J. Kroupa, J. Prokleška, K. Chapagain, B. Dabrowski, and V. Goian, Phys. Rev. B **95**, 174103 (2017).
[36] S. H. Skjærvø, Q. N. Meier, M. Feygenson, N. A. Spaldin, S. J. L. Billinge, E. S. Bozin, and S. M. Selbach, Phys. Rev. X **9**, 031001 (2019).
[37] S. Artyukhin, K. T. Delaney, N. A. Spaldin, and M. Mostovoy, Nat. Mater. **13**, 42 (2014).

[38] See Supplemental Material at http://link.aps.org/supplemental/10.1103/PhysRevB.103.024101 for model parameters and the improper FE nature shown by our first-principles calculations.
[39] G. Kresse and J. Furthmüller, Phys. Rev. B **54**, 11169 (1996).
[40] G. Kresse and J. Furthmüller, Comput. Mater. Sci. **6**, 15 (1996).
[41] G. I. Csonka, J. P. Perdew, A. Ruzsinszky, P. H. T. Philipsen, S. Lebègue, J. Paier, O. A. Vydrov, and J. G. Ángyán, Phys. Rev. B **79**, 155107 (2009).
[42] S. L. Dudarev, G. A. Botton, S. Y. Savrasov, C. J. Humphreys, and A. P. Sutton, Phys. Rev. B **57**, 1505 (1998).
[43] M. Cococcioni and S. de Gironcoli, Phys. Rev. B **71**, 035105 (2005).
[44] A. Togo and I. Tanaka, Scr. Mater. **108**, 1 (2015).
[45] R. P. Feynman, A. R. Hibbs, and D. F. Styer, *Quantum Mechanics and Path Integrals* (Courier, North Chelmsford, MA, 2010).
[46] D. M. Ceperley, Rev. Mod. Phys. **67**, 279 (1995).
[47] D. M. Juraschek, Q. N. Meier, and P. Narang, Phys. Rev. Lett. **124**, 117401 (2020).